

Demonstration of Fused RTK (Fixed) + Inertial Positioning Using Android Smartphone Sensors Only

1st Mohamed Bochkati

*Institute of Space Technology and Space Applications
Bundeswehr University Munich
Neubiberg, Germany
mohamed.bochkati@unibw.de*

2nd Himanshu Sharma

*Institute of Space Technology and Space Applications
Bundeswehr University Munich
Neubiberg, Germany
himanshu.sharma@unibw.de*

3rd Christian A. Lichtenberger

*Institute of Space Technology and Space Applications
Bundeswehr University Munich
Neubiberg, Germany
christian.lichtenberger@unibw.de*

4th Thomas Pany

*Institute of Space Technology and Space Applications
Bundeswehr University Munich
Neubiberg, Germany
thomas.pany@unibw.de*

Abstract—This paper describes several experiments related to centimeter accurate positioning using the build-in GNSS receiver and inertial measurement unit (IMU) of a dual-frequency commercial smartphone. Using a choke-ring antenna platform to shield the smartphone from the ground multipath we were able to obtain a GNSS carrier phase (GPS+Galileo L1/L5) solution with good fixed ambiguities and approx. 2 centimeter precision. Furthermore, the GNSS antenna phase center (APC) within the smartphone was determined. An Allan variance analysis of the inertial measurement unit shows an unexpected good gyro bias instability of approx. 15 deg/h. An integrated real-time kinematic (RTK) GNSS+IMU solution was computed and a heuristic sensitivity analysis was performed.

Keywords—GNSS, smartphone, RTK, inertial navigation, mass-market; smartphone antenna phase center

I. INTRODUCTION

Performing RTK with the smartphone using GNSS raw measurement is one of the most eminent topic of research in GNSS navigation community in the past 4-5 years. Location-based service (LBS) using smartphone covers more than 45 % of the GNSS equipped devices available in the market [1]. With dual-frequency GNSS chips inside smartphones, the position accuracy has been improved from 8-10 meters to 1-2 meters under good environmental conditions [2]. Under the influence of multipath, the use of L5 signal is expected to improve the receiver performance. But, to cope up with the technical advancement like augmented reality (AR) and autonomous driving (AD), decimeter-level accuracy is not sufficient. The centimeter-level accuracy using RTK comes at the cost of high quality carrier phase measurements, which are said to be the heart of RTK positioning technique. But, with the poor quality of GNSS antenna, low quality temperature compensated crystal oscillator (TCXO) used for driving smart-

phone internal clock, optimized tracking loops for pseudorange instead of carrier phase, and power optimization using duty cycling, the quality of carrier phase is extremely degraded and does not sustain for good RTK solution. In 2018, we demonstrated that the GNSS chip (BCM47755) inside the Xiaomi Mi 8 smartphone is from the technical side good enough to provide quality carrier phase measurement, using a better quality of antenna as an input source [2]. Furthermore, we also investigated that the multipath mitigation using choke-ring platform, also smooths the carrier phase measurement and provides high ambiguity fixing rate without any external antenna [3]. In one of the most recent publications that deal with dual-frequency mobile phones [4], researchers were able to demonstrate centimeter-accurate position determination with observations of the dual-frequency *Huawei P30* smartphone. However, the successful ambiguity fixing could be performed only on GPS L1, i.e. no dual-frequency carrier phase fixing was feasible. Moreover, a relative antenna calibration (w.r.t. well calibrated geodetic antenna) for GPS L1 only has been conducted, which revealed that the horizontal phase center offsets from the central vertical axis of the smartphone and also the phase center variations do not exceed 1–2 cm.

In this contribution, we conducted different experiments to explore the accuracy that can be achieved by using dual-frequency consumer portable device. These experiments deal with both smartphone built-in GNSS and IMU sensors and cover static as well as kinematic scenarios which are partly linked to each other.

The remainder of this paper is structured as follows. Section II describes the stochastic error modeling of the built-in Mi 8 smartphone IMU using both Allan variance technique and the autocorrelation function. Afterwards, the estimated parameters are employed to perform different RTK-IMU fusion scenarios

which highlight the capability of smartphones in term of navigation performance. Here, only float RTK solution has been achieved. Since the ambiguity term could not be resolved properly due to the quality of the GNSS observations where the multipath factor is assumed to have the main impact, we dedicate section III to investigate the behavior of the GNSS data obtained by such devices in a static scenario. A test with a choke-ring platform provides a fixing rate of 89% which validates these assumptions. This unprecedented accuracy paved the way to conduct different test campaigns in order to determine the APC of the smartphone.

II. STOCHASTIC ERROR MODELING OF THE SMARTPHONE INERTIAL SENSORS

In order to make the smartphone IMU signals useful for navigation, both stochastic modeling and calibration procedures, e.g. six-position static test [5], of the sensor inherent errors are mandatory. The derived parameters such as the spectral density of the noise processes or the bias and scale factor (SF) can then be fed to the INS (inertial navigation system)/GNSS fusion algorithm (usually Kalman filter). In this contribution, we used the post-processing commercial software from NovAtel Inc. “*Inertial Explorer, version 8.70.8722*” to combine GNSS and IMU. As per default, this software contains different IMU profiles (customers IMUs) that can be easily used to perform the fusion process, which is a very effective way to achieve in a short time meaningful navigation results (position, velocity and attitude information). Nevertheless, this requires from the user to have one of these devices already included in this software. But, when it comes to the employment of a new IMU device the task of defining the appropriate profile becomes very challenging as the calibration procedures are very time consuming. To this end, a static data set from three Mi 8 smartphones have been collected using in-house developed ISTA-Logger, which represents an extension of the Google Android GNSS-Logger [6] with an additional interface to access other smartphone sensors such as accelerometer, gyroscope or magnetometer. For comparison reasons, a commercial IMU from the Xsens company (*MTi-G-710* [7]) was running in the same time. The total measurement time was around 1 hour. To make sure that there is no influence from the environment, the sensors were located in a room with constant temperature. The sampling rates of all devices were set up to be approx. 400 Hz, which is the maximum sampling rates that the Mi 8 Android logger can achieve. Of course, this value depends on the type of smartphone under investigation and also the used Android command to retrieve the IMU raw measurements which has been set in our Logger as “SENSE_DELAY_FASTEST” [8]. To explore the stochastic behavior of each device, the Allan variance technique [9] has been used. According to this methodology, the parameters of the stochastic processes can be identified by a specific slope within a logarithmic plot. In the IEEE standards document [10] various random processes are described in details which are summarized synthetically in Fig. 1. For instance, the white noise spectral density parameter can

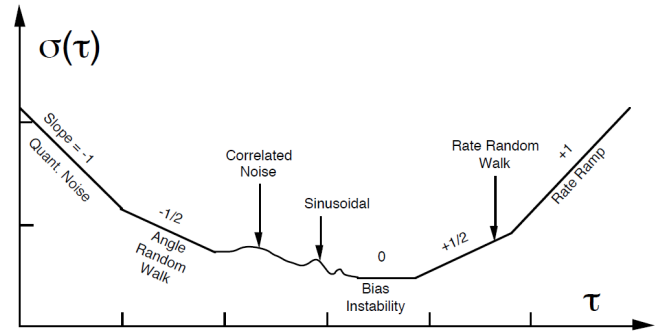


Fig. 1: Sample plot of Allan variance analysis results [10]

be estimated at the the proper cluster time (for us $\tau = 1$ s in Fig. 2 and Fig. 7) where the slope of the curve is equal to $-1/2$. This parameter is called in conjunction with accelerometer and gyroscope, velocity random walk (VRW) and angle random walk (ARW), respectively. An other parameter that cannot be ignored is the so-called bias instability (in term of oscillator is the flicker noise [9]) which has a slope of zero, i.e. the flat region that this curve exhibits. Please note that in [10] there is no recommendation at which τ exactly the bias instability term can be read off. In general, special care should be taken when investigating the stochastic behavior of IMU signals by means of this technique, since in practice the error sequence showed in this diagram can deviate from the synthetic representation in Fig. 1

Taking this generalized diagram of all random processes in mind, we can see that the incorporated smartphone accelerometer axes contain white noise, bias instability (BI) and correlated noise (Fig. 2). In comparison to the Xsens IMU, the axis of the Mi 8 accelerometer random processes are not identical, especially the z-axis which reflects the exact behavior of correlated noise. The latter can be modeled as 1st-order Gauss-Markov (GM) process. According to [11], the Gauss-Markov process is a random quantity whose autocorrelation function is a decreasing exponential.

$$R_{xx}(\tau) = \sigma^2 e^{-\beta|\tau_{corr}|} \quad (1)$$

where β and σ are the inverse of correlation time τ_{corr} and the standard deviation of the process, respectively. These characteristics are summarized in Fig. 3. The time continuous equation of the GM-process can be written as

$$\dot{x}(t) = -\beta x(t) + \sqrt{2\sigma^2\beta}w(t) \quad (2)$$

Astonishingly, all three smartphones have the same behavior in the z-axis. To explain this behavior in terms of numbers, the auto correlation sequence $R_{xx}(\tau)$ for this axis has been generated, as depicted in Fig. 4 to 6. Referring to the synthetic representation of the random process in Fig.1 and Fig. 3, the related standard deviation can be read off by σ^2/e (intersection of the dotted lines in each plot), thus the correspondent correlation time is the projection of this value onto the x-axis [12]. As summarized in Table I the standard deviation of the

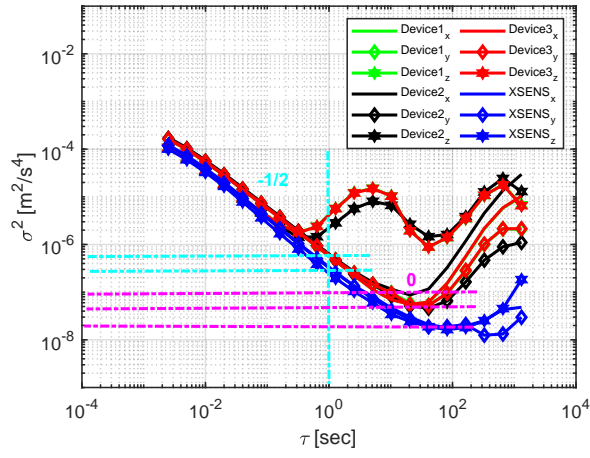


Fig. 2: Allan variance results for all used accelerometers

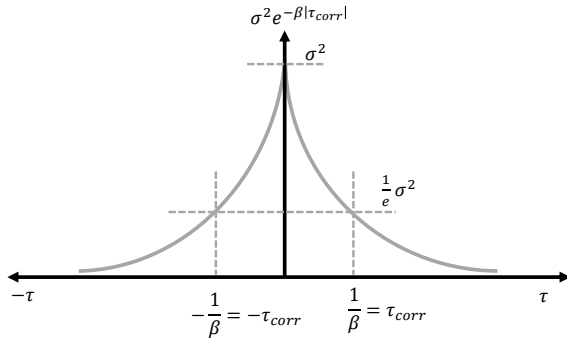


Fig. 3: Autocorrelation sequence of the first-order GM process

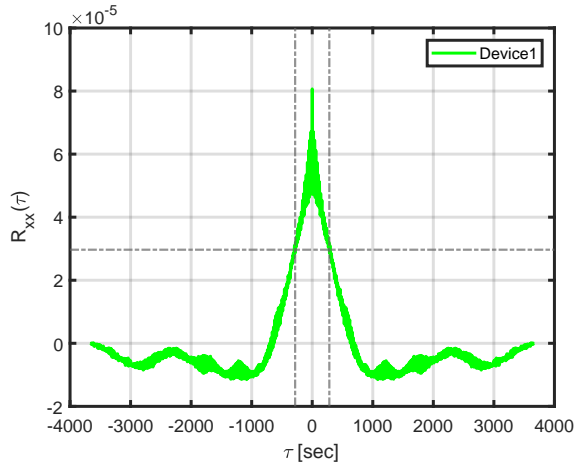


Fig. 4: Autocorrelation sequence of the accelerometer z-axis for the Mi 8 device $n^{\circ}1$

GM-process and its correlation time τ_{corr} are between $550 \mu g$ and $580 \mu g$ @ $\tau_{corr} = 282 s$ and $\tau_{corr} = 398 s$. Both x- and y-axis are mainly corrupted by white noise and bias instability. For example, the white noise power spectral density of the VRW is approx. $80 \mu g/\sqrt{Hz}$. On the other side, the Xsens accelerometer exhibits the same fluctuation in all axis, i.e. all

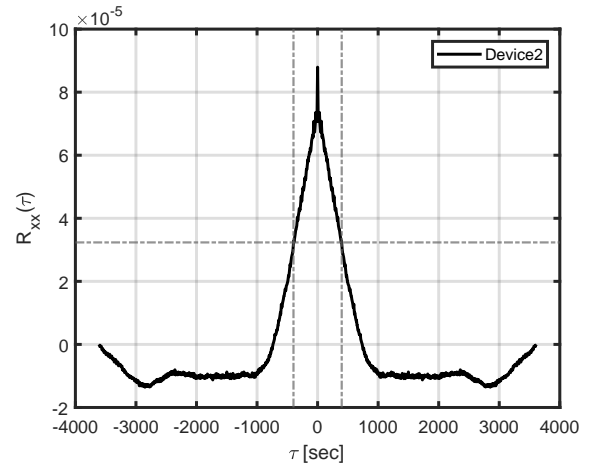


Fig. 5: Autocorrelation sequence of the accelerometer z-axis for the Mi 8 device $n^{\circ}1$

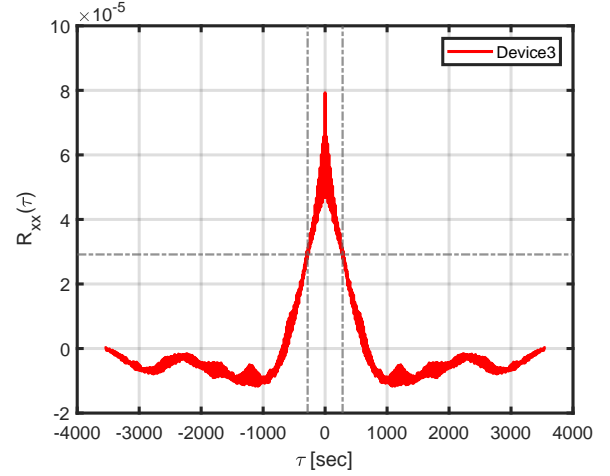


Fig. 6: Autocorrelation sequence of the accelerometer z-axis for the Mi 8 device $n^{\circ}1$

three axes are symmetrical. Here, for example, the estimated velocity random walk (VRW) values are almost identical and can be verified by the manufacturer specifications [7].

From the gyroscope side, it is well known that its stochastic characteristics dictate the accuracy of the strapdown computation. This is due to fact that the gyro observations i.e. the angular rates or angular increments (in case of integrating gyroscope [13]) are used to transform the measured specific force (by the accelerometer) from the body-frame to the navigation frame, e.g. n-frame, where the navigation process is usually expressed. Moreover, during the strapdown integration, the sensed angular rates (incl. both constant and random errors) undergo the integration three times (t^3) to deliver absolute attitude information, whereas the specific force is integrated twice to provide both position and velocity components.

The Allan variance diagram in Fig. 7 shows the same noise fluctuation for all axes and reveals in the same time, unexpected, less noise within the Mi 8-IMUs. From Table II we

TABLE I: Estimated noise coefficients using the output signal of the accelerometers

Device		VRW [$\mu\text{g}/\sqrt{\text{Hz}}$]	BI [μg]	1st-Order GM [μg]
Mi 8 n°1	X	78	39.1	\emptyset
	Y	79	42.5	\emptyset
	Z	\emptyset	\emptyset	555.5 @ $\tau_{corr} = 282.4 \text{ s}$
Mi 8 n°2	X	81	46.0	\emptyset
	Y	79	33.0	\emptyset
	Z	\emptyset	\emptyset	579.9 @ $\tau_{corr} = 398.3 \text{ s}$
Mi 8 n°3	X	77	36.1	\emptyset
	Y	79	34.8	\emptyset
	Z	\emptyset	\emptyset	550.5 @ $\tau_{corr} = 282 \text{ s}$
MTi-G-710	X	59	20.6	\emptyset
	Y	57	20.9	\emptyset
	Z	50	19.6	\emptyset

can see, that both ARW and bias instability BI values of the all three smartphone gyros are smaller then those of the commercial Xsens device. In details, in the case of the Mi 8 gyro, the angle random walk parameters are smaller then $0.31 \text{ deg}/\sqrt{\text{h}}$, while the Xsens indicates amplitudes between $0.49 \text{ deg}/\sqrt{\text{h}}$ and $0.55 \text{ deg}/\sqrt{\text{h}}$. Additionally, it can be seen that within one smartphone the noise level of the three gyroscope axes is different, especially the less random walk noise and bias instability error affecting the z-axis. Here, the ARW and the BI in x- and y-direction have a mean of $0.27 \text{ deg}/\sqrt{\text{h}}$ (ARW) and $14.2 \text{ deg}/\text{h}$ (BI), respectively. On the hand, the z-axes indicate a mean value of both $0.18 \text{ deg}/\sqrt{\text{h}}$ and $9.2 \text{ deg}/\text{h}$, which can have a positive contribution in determining the heading angle.

A satisfying explanation of this unforeseen random behavior of the Xiaomi Mi 8 z-axis can be found in the manufacturing process related to the MEMS (Micro Electro Mechanical System) technology. A three-axis MEMS accelerometer chip is able to sense accelerations as a reaction of the force applied to the chip housing. The change in movement is equivalent to the change of capacitance between the moving structure of the chip. To guarantee the sensitivity in all three directions, i.e. x,y and z, two proof masses are available, namely a XY-axis proof mass and Z-axis proof mass that detect the in-plane and out-of-plane accelerations respectively [14], [15]. But, due to the limited space in a smartphone, the manufacture usually tends to use only one MEMS-chip. In contrast to the Mi 8 smartphones, the Xsens-IMU comprises a set of three MEMS accelerometer chips orthogonally arranged to provide acceleration signal in all three directions which explains the similar noise figure observed in Fig. 2.

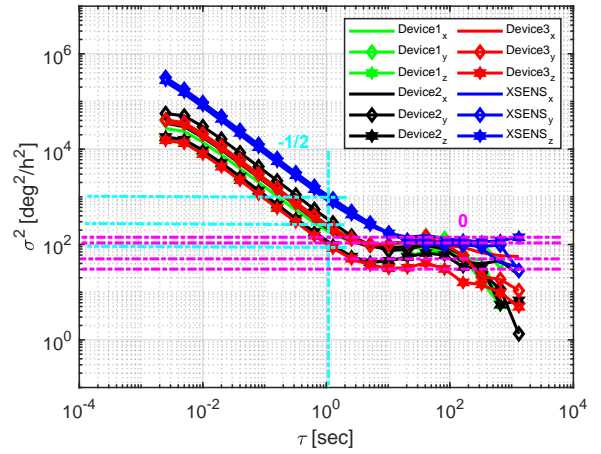


Fig. 7: Allan variance results for all used gyroscopes

TABLE II: Estimated noise coefficients using the output signal of the gyroscopes

Device		ARW [$\text{deg}/\sqrt{\text{h}}$]	BI [deg/h]
Mi 8 n°1	X	0.23	13.8
	Y	0.27	14.8
	Z	0.18	9.7
Mi 8 n°2	X	0.25	13.9
	Y	0.31	13.1
	Z	0.18	9.6
Mi 8 n°3	X	0.26	14.7
	Y	0.27	14.9
	Z	0.17	8.5
MTi-G-710	X	0.49	18.0
	Y	0.55	15.1
	Z	0.51	15.6

III. RTK/INS SMARTPHONE-BASED SENSOR FUSION

A. Experimental Setup

To highlight the benefit of aiding the RTK smartphone positioning with the built-in MEMS IMU, we conducted an experiment with a moving vehicular platform (see Fig. 8) in March 2019. This experiment comprises the following setup: a dual-frequency (L1/E1 and L5/E5A) Xiaomi Mi 8 smartphone placed on the roof of the car (backside). Similarly, for comparison purposes, we placed underneath the Mi 8 the same Xsens IMU as used in the previous experiment. In the front, a Trimble Zephyr 2 geodetic antenna was connected to a Trimble NetR9 receiver which serves as reference. During the whole measurement campaign, the test vehicle had a moderate constant speed of approx. 30 km/h. We chose the campus of our university to conduct this experiment. During the measurement campaign, the satellite visibility was not always optimal due to existing high buildings, with an elevation of up to 70° , which might have blocked/reflected the incoming

GNSS signals can thus jeopardize the carrier-phase positioning or even make it impossible for several epochs. Both GNSS and IMU smartphone observations were collected using the ISTA-Logger with 1 Hz and 400 Hz, respectively. The Xsens IMU was connected via USB to a laptop in order to log the raw data with 400 Hz sampling rates, while the Trimble NetR9 receiver saves every second the GNSS observation internally. To enable the carrier phase positioning, a reference station located on top of the highest building in the campus was running during the measurement campaign. The duration of the trajectory was around 15 minutes.

To exploit the maximum performance that can be obtained with poor-quality GNSS data we employed the post-processing commercial software from NovAtel Inc. "*Inertial Explorer, version 8.70.8722*". After pre-processing the collected raw data and converting the IMU raw observations of both Mi 8 and Xsens to the required binary format of the used software, we generated the appropriate IMU profiles based on Table I and Table II. Afterwards, different coupling scenarios have been performed based on the Loosely-Coupled (LC) strategy [13]. Exactly speaking, three scenarios were conducted: First computing a pure smartphone and a pure Trimble solution as for the LC the GNSS solution should be processed, independently, in advance. Secondly, aiding the commercial grade GNSS receiver with either Xsens IMU or Mi 8 IMU observations. In the final step, aiding the Mi 8 GNSS measurements with either Xsens or the internal IMU data. An overview about these different combination can be found in Table III.

B. Experiment Results

Since we are dealing with RTK positioning, the success rates of RTK carrier-phase fixing should be first investigated carefully. In this part, a special attention should be given to the contribution of the IMU devices improving the fixing ratio of this important term. From Table III, it is clear that the Xiaomi Mi 8 smartphone is providing only float solution accompanied with meter-accuracy position, even if the GNSS observation have been supported by both IMUs, i.e. Xsens- and Mi 8 IMU. The main reason for this unsatisfactory results is inherent in the limited capability of the low-cost smartphone GNSS antenna to suppress the noise as well as the reflected signals from the surrounding. Nonetheless, ways to achieve high fixing ratio (up to 95 %) with Mi 8 GNSS data will be discussed in Section IV and V. And as we are performing LC between the GNSS and the IMU observations, the IMU is not able to deliver a meaningful improvement to the fixing of the ambiguity terms. This statement can be proven by observing the RTK fixing ratio based on the Trimble receiver where 91 % and 92 % for GNSS only and GNSS+IMU has been achieved, respectively. This tiny difference, i.e. 1 %, cannot be seen as a real improvement from the IMU since it could be a wrong fixing caused by the used commercial software of NovAtel.

Bearing this in mind, a further comparison and analysis are worthy. To this end, we consider the Trimble-Xsens LC-solution, i.e. position, velocity and attitude information, as ground truth. The deviation of the other navigation solution

(relative accuracy), i.e. either GNSS only or LC GNSS/IMU, as stated in Table III w.r.t. this reference trajectory will be computed and discussed. Therefore, all navigation results have been reduced to the origin of the reference scenario which refers to the origin of the body-frame of the Xsens IMU. For better interpretation of the results, we denote in general the deviation with the following symbol δ . Thereby, five differences can be generated as we have six solutions and one of them represents the truth. Thus the comparison will be done according to the following order:

- 1) Trimble-Xsens vs. MI8-MI8
- 2) Trimble-Xsens vs. MI8-Only
- 3) Trimble-Xsens vs. MI8-Xsens
- 4) Trimble-Xsens vs. Trimble-MI8
- 5) Trimble-Xsens vs. Trimble-Only

Due to the fact that a standalone GNSS is not able to provide the fully three dimensional attitude information, the obtained orientation angles, i.e. heading (ψ), roll (ϕ) and pitch (θ) will be compared only in the case of LC strategy.

In Fig. 9 and Fig. 10 the horizontal trajectory components (east vs. north) and the corresponding height are depicted, respectively. Considering the ground truth trajectory, i.e. Trimble-Xsens, we can see that the Mi 8 GNSS only solution (MI8-Only) jumps up and down around the reference but it is able to follow the right track. After including the IMU observations (MI8-MI8 or MI8-Xsens) the GNSS position becomes smoother (interpolation with higher sampling rates of the IMU), but in some parts of the trajectory (for instance left upper part of Fig. 9) these two scenarios did not meet the expected performance. As indicated in Table IV to Table VI, the mean deviation for MI8-MI8 ($\delta N_1 = 3.401$ m) and MI8-Xsens ($\delta N_3 = 3.517$ m) is larger than the difference of the Mi 8 GNSS only scenario, i.e. δN_2 . Both east and height show similar behavior, i.e. the mean difference of the MI8-Only scenario is at least one order of magnitude smaller than with IMU. One possible explanation for this issue can be hidden in the weighting between the GNSS and the IMU observation within the Kalman filter, which is usually realized by the so-called Kalman gain matrix \mathbf{K} [11]. As mentioned before, we considered only the stochastic errors in generating the appropriate IMU profiles for *Inertial Explorer*. The constant term such as bias and scale factor were not included in this performance evaluation. As expected, the Trimble-Only example provides the smallest errors, i.e. $\delta N_5 = 0.011$ m, $\delta E_5 = 0.017$ m and $\delta H_5 = 0.028$ m. On the other side, the relative error obtained from Trimble-MI8 is in the east as well as in the north direction at the decimeter level. This is due to the fact that the lever-arm between the antenna reference point (ARP) of the Trimble receiver and the origin of the Xsens IMU can be calibrated with high accuracy (mm-accuracy), whereas in the case of the MEMS Mi 8, the origin of the b-frame is located somewhere in the smartphone housing which makes the lever-arm uncertainty in the range of the smartphone dimension. Nevertheless, these results indicate that the Mi 8 IMU can be used for sensor fusion purposes, but it requires in the same

TABLE III: RTK fixing ratio generated from different GNSS/IMU combinations

GNSS	IMU		
	Xiaomi Mi 8	XSENS	NONE
Xiaomi Mi 8	0%	0%	0%
Trimble NetR9	92%	92%	91%

time high quality GNSS signals to bound the drift due to other uncompensated errors.

As illustrated in Fig. 11 to Fig. 13, the velocity profiles expressed in the ENU (East-North-Up)-frame (navigation frame employed by *Inertial Explorer*, where the y-axis points to the true north, x-axis to the east and the z-axis completes the right handed coordinate system [16]) show a smooth behaviors, apart from the GNSS only solution with Trimble and Mi 8 where some remarkable spikes by second 300 and 600 are available. Exactly at this time, because of the surrounding high buildings, the observed GNSS satellites were not sufficient to provide navigation information. These spikes disappear after introducing the IMU signal. The statistics related to the relative velocity error are summarized in Table VII, Table VIII and Table VII. These results confirm the analysis made for the position coordinates.

In term of attitude angles, the heading information derived from MI8-MI8, Trimble-MI8 and Trimble-Xsens scenario exhibit the same course (Fig. 14). However, the heading angle of the MI8-Xsens is somehow delayed by approx. 180° , which cannot be explained. In general, these results are not reliable enough (see statistics in Table X), as with MEMS devices only a kinematic alignment is possible [17] where the GNSS north/ east velocities (Doppler information) are introduced to initialize the heading angle. In the case of the Mi 8 GNSS chip, without further protection from ground multipath, only float RTK ambiguities are available which degrades the navigation accuracy immensely. Thus, the introduced velocity information have almost no contribution to the navigation performance. On the other hand, the roll and pitch angles can be initialized in static or kinematic mode. The drift of these angles are, however, bounded by the so-called *Schuler* period (≈ 84 minutes) [13]. The pitch angles obtained by fusing the of Mi 8 GNSS observation with the Xsens IMU signal look different from the other combinations especially in the static phases at the beginning and at the end of the trajectory, where this angle drifts slightly even though GNSS support is available. The problem here could be the drift of the bias which cannot be corrected properly by the estimation filter.

IV. IMPACT OF GROUND MULTIPATH ON THE SMARTPHONE RTK AMBIGUITY FIXING

The smartphone GNSS antenna is a less than 1 dollar antenna with low multipath mitigation capability. The work presented in [2] has already demonstrated that using a good quality antenna with high multipath mitigation performance,

TABLE IV: Deviation of the north coordinates from the ground truth solution (Trimble-Xsens)

	δN_1 [m]	δN_2 [m]	δN_3 [m]	δN_4 [m]	δN_5 [m]
Mean	3.401	-1.038	3.517	0.208	0.011
Max	47.265	24.110	43.853	0.598	0.519
Min	-28.442	-20.373	-25.495	-0.562	-1.363

TABLE V: Deviation of the east coordinates from the ground truth solution (Trimble-Xsens)

	δE_1 [m]	δE_2 [m]	δE_3 [m]	δE_4 [m]	δE_5 [m]
Mean	-5.239	0.328	-5.105	0.074	0.017
Max	15.547	9.742	14.346	0.438	0.806
Min	-28.781	-15.624	-32.369	-0.640	-0.566

TABLE VI: Deviation of the height coordinates from the ground truth solution (Trimble-Xsens)

	δH_1 [m]	δH_2 [m]	δH_3 [m]	δH_4 [m]	δH_5 [m]
Mean	9.780	0.690	7.862	0.010	0.028
Max	38.407	20.242	40.439	0.065	1.981
Min	-3.054	-28.600	-6.368	-0.151	-0.035

TABLE VII: Deviation of the north velocity from the ground truth solution (Trimble-Xsens)

	δV_{N1} [m/s]	δV_{N2} [m/s]	δV_{N3} [m/s]	δV_{N4} [m/s]	δV_{N5} [m/s]
Mean	0.01	0.04	0.01	0.01	0.06
Max	2.82	6.71	5.64	0.56	22.02
Min	-2.07	-3.34	-3.00	-0.46	-19.12

cm-level RTK accuracy is possible using raw GNSS measurements from smartphones. In order to achieve this level of accuracy with the smartphone quality antenna, it is essential to determine the APC location precisely and also minimize the effect of multipath on the carrier-phase measurements. But, due to the poor quality of this observation type, smartphone antenna calibration with the anechoic chamber [18] or by using automatic robot arm to rotate the antenna [19] becomes very tedious. However, the choke-ring platforms have been studied over several decades and proved to be very effective

TABLE VIII: Deviation of the east velocity from the ground truth solution (Trimble-Xsens)

	δV_{E1} [m/s]	δV_{E2} [m/s]	δV_{E3} [m/s]	δV_{E4} [m/s]	δV_{E5} [m/s]
Mean	0.01	0.05	-0.01	0.01	-0.02
Max	1.19	2.57	2.09	0.36	11.59
Min	-1.36	-1.90	-1.48	-0.44	-16.86

TABLE IX: Deviation of the up velocity from the ground truth solution (Trimble-Xsens)

	δV_{U1} [m/s]	δV_{U2} [m/s]	δV_{U3} [m/s]	δV_{U4} [m/s]	δV_{U5} [m/s]
Mean	-0.01	-0.08	-0.01	0.01	-0.10
Max	0.99	3.48	1.10	0.47	28.96
Min	-1.03	-3.95	-1.25	-0.26	-37.16

TABLE X: Deviation of the heading angles from the ground truth solution (Trimble-Xsens)

	$\delta \psi_1$ [deg]	$\delta \psi_2$ [deg]	$\delta \psi_3$ [deg]	$\delta \psi_4$ [deg]	$\delta \psi_5$ [deg]
Mean	-14.244	\emptyset	-49.117	-24.829	\emptyset
Max	355.989	\emptyset	318.946	347.558	\emptyset
Min	-353.167	\emptyset	-337.490	-355.142	\emptyset

TABLE XI: Deviation of the roll angles from the ground truth solution (Trimble-Xsens)

	$\delta \phi_1$ [deg]	$\delta \phi_2$ [deg]	$\delta \phi_3$ [deg]	$\delta \phi_4$ [deg]	$\delta \phi_5$ [deg]
Mean	1.662	\emptyset	0.806	1.448	\emptyset
Max	15.376	\emptyset	9.929	12.490	\emptyset
Min	-10.803	\emptyset	-7.843	-10.034	\emptyset

again multipath originating from the surface just below the antenna. Such hardware belongs usually to the main setup of high precise geodetic GNSS networks which helps to keep the required mm-accuracy of reference coordinates immensely. In order to demonstrate the effectiveness of using a choke-ring to shield such low-cost device, series of experiments were performed with Xiaomi Mi 8 smartphone placed on choke-ring platform, as depicted in Fig 17, while logging the GNSS observations. In the vicinity, another Xiaomi Mi 8 smartphone was placed without any choke-ring (Fig. 17) to show the

TABLE XII: Deviation of the pitch angles from the ground truth solution (Trimble-Xsens)

	$\delta \theta_1$ [deg]	$\delta \theta_2$ [deg]	$\delta \theta_3$ [deg]	$\delta \theta_4$ [deg]	$\delta \theta_5$ [deg]
Mean	-0.393	\emptyset	-0.006	0.713	\emptyset
Max	5.739	\emptyset	7.537	7.662	\emptyset
Min	-8.001	\emptyset	-7.049	-7.182	\emptyset

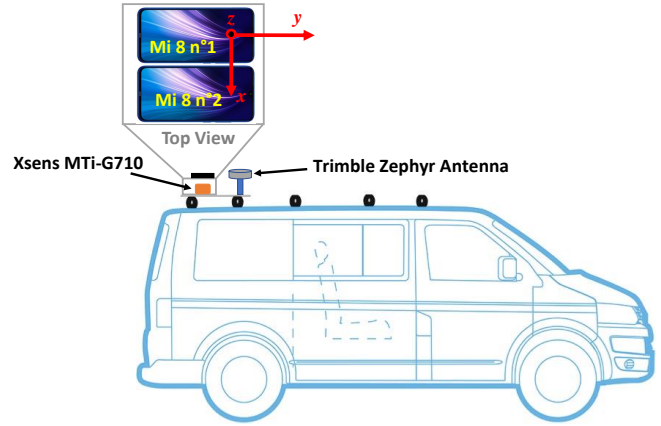


Fig. 8: Experiment setup with Xiaomi Mi 8 smartphones on top

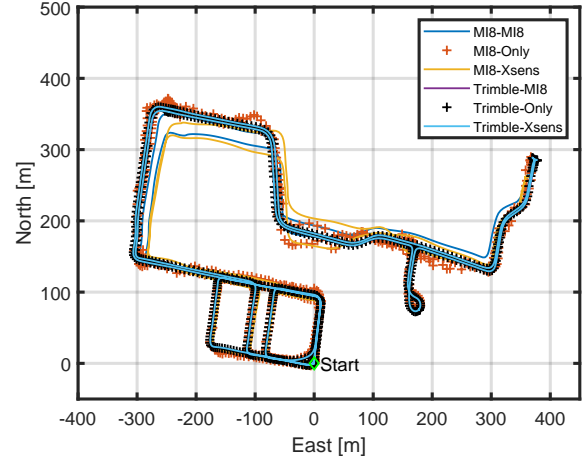


Fig. 9: Computed trajectory using different sensor combinations in ENU-frame

comparison. Both smartphones use geodetic pillars with highly precise (mm-accuracy) coordinates as reference. With both devices, two RINEX (Receiver Independent Exchange Format) files containing the GNSS observations have been recorded for about 1 hour.

The positioning result with the choke-ring platform shows a significant improvement in the positioning accuracy in comparison to Mi 8 without choke-ring platform as shown in

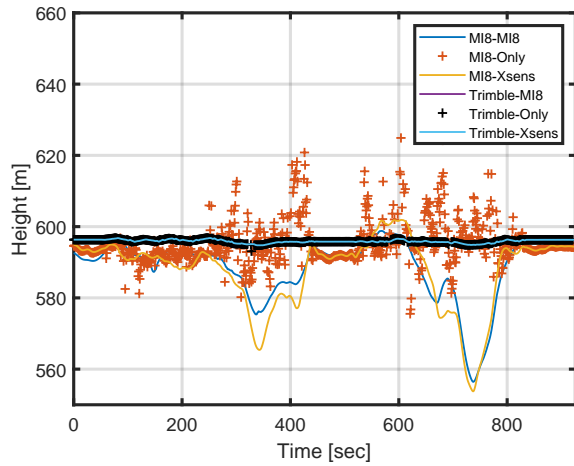


Fig. 10: Computed height using different sensor combinations in ENU-frame

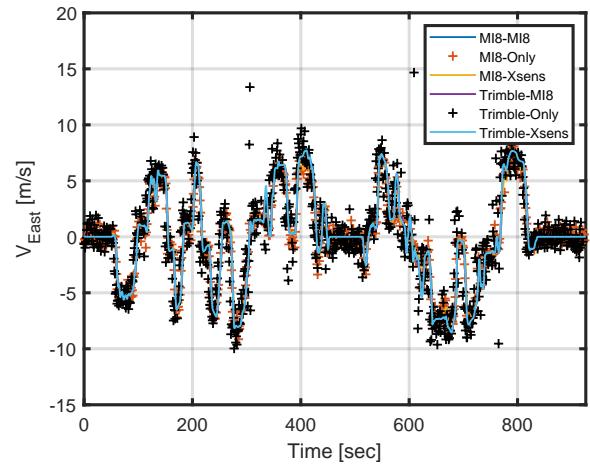


Fig. 12: Computed east velocity using different sensor combinations in ENU-frame

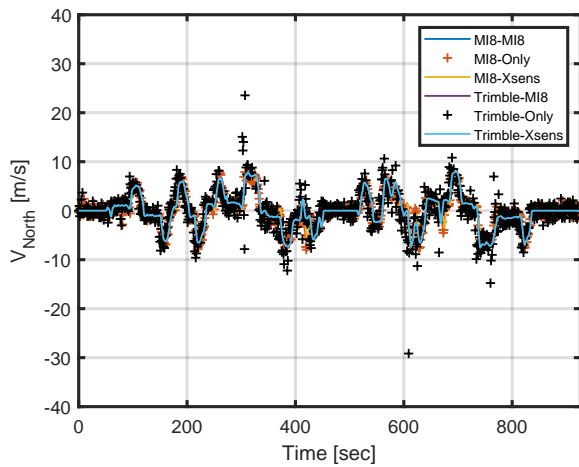


Fig. 11: Computed north velocity using different sensor combinations in ENU-frame

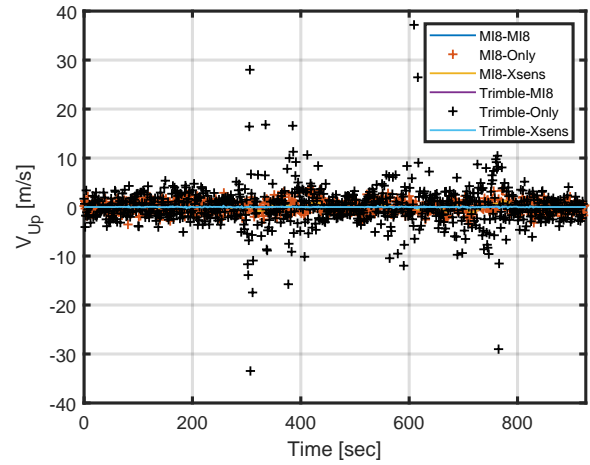


Fig. 13: Computed up velocity using different sensor combinations in ENU-frame

Fig. 18-19 .

The RTK position analysis of GNSS observation data without choke-ring was performed first. The mean error in the position, expressed in the earth-centered, earth-fixed frame (ECEF), w.r.t. to true coordinates of the geodetic pillar were calculated as 0.462 m, 0.034 m and 2.921 m in x , y and z , respectively (see Fig. 19). On the other side, position accuracy with the Mi 8 smartphone kept on the choke-ring platform shows mean position error of 0.041 m, 0.032 m and 0.035 m in x , y and z , respectively (see Fig. 18).

In addition to the static case, we performed a dynamic measurement by placing both smartphone and choke-ring on a rotating platform [20], as depicted in Fig. 20. During this experiment the platform was rotating at very low speed while the Xiaomi Mi 8 was logging raw GNSS observations using the *Geo++ RINEX Logger* (version 2.1.5) Android application [21]. Simultaneously, a high quality GNSS receiver + antenna,

Trimble R10, was located nearby (a few meters away) to serve as a reference. Using the GNSS observation collected by the Trimble R10 as well as the rotated smartphone + choke-ring, RTK was performed by means of the *Inertial Explorer* software package. As depicted in Fig. 21, the result plots clearly show high ambiguity fixing of the smartphone carrier phase up to 89% with an accuracy level of 1-2 cm with circle as a reference trajectory. However, the APC is still unknown and could contribute further improvement up to the cm-level.

V. DETERMINATION OF XIAOMI MI 8 ANTENNA PHASE CENTER

In the previous section we have shown that it is possible to estimate RTK fixed solution with the dual-frequency Xiaomi Mi 8 smartphone mounted on a choke-ring. In conjunction with this experiment, the investigation of the characteristics of the APC could be initiated. As stated before, another pragmatic advantage is the possibility of performing absolute positioning

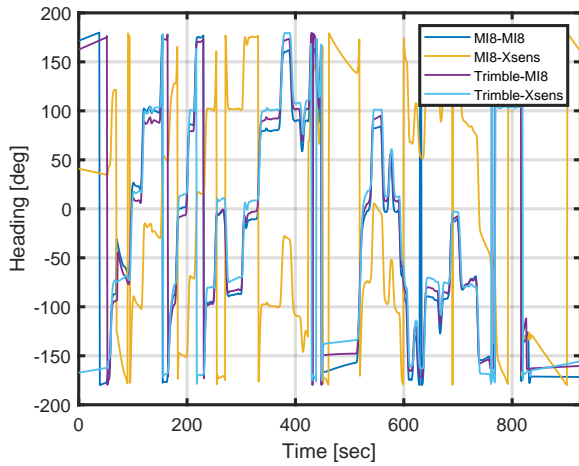


Fig. 14: Computed heading angle using different sensor combinations in ENU-frame

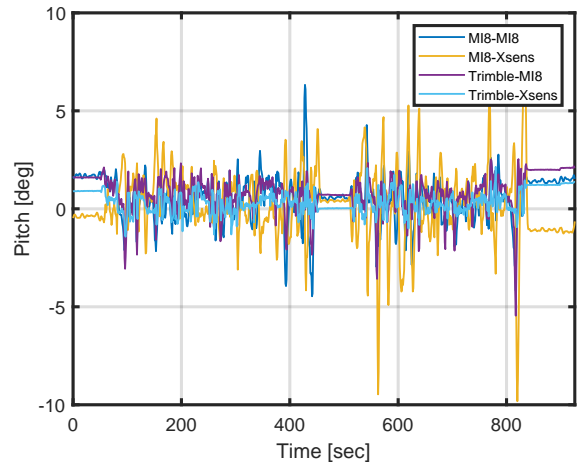


Fig. 16: Computed pitch angle using different sensor combinations in ENU-frame

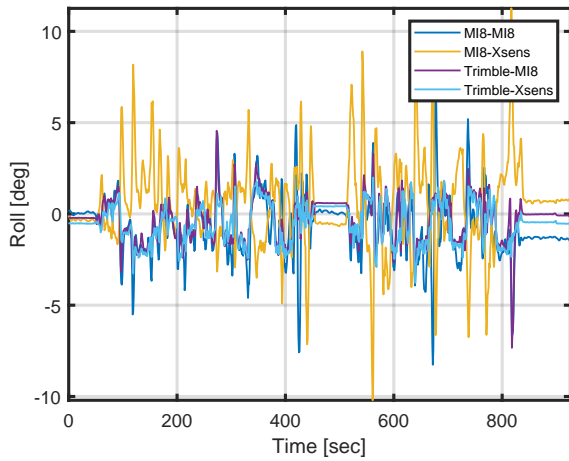


Fig. 15: Computed roll angle using different sensor combinations in ENU-frame

with smartphones in the centimeter range. Usually, GNSS user equipment determines a navigation solution for a particular point in space, known as antenna phase center (APC). This point does not necessarily coincide with the physical center of the antenna and may even be outside the antenna casing [17]. In such cases, the determination of the phase center becomes really challenging. For this reason, a first test setup was designed to estimate the APC relative to the smartphone geometry. Herein, we propose a straightforward method to determine the APC location which consists of combining terrestrial measurements as used in the surveying field (for determining the geometry and orientation of the smartphone) and GNSS observations, assumed, received at the APC. This approach stipulates that the measurements of both employed surveying instrument and the computed cm-accurate Mi 8 RTK-positions are expressed in the same geodetic reference frame. Furthermore, the position and the orientation of the



Fig. 17: Xiaomi Mi 8 smartphone with (left) and without choke-ring (right)

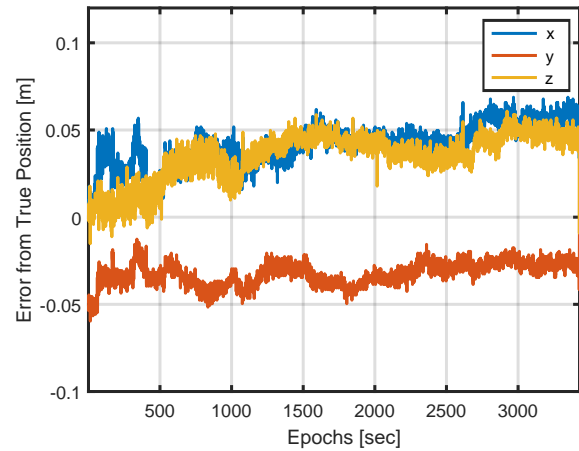


Fig. 18: RTK-Position error of Mi 8 placed on a choke-ring

smartphone housing (corners) should be precisely known also in the same frame, which can be measured with mm-accuracy by means of the surveying apparatus. In the following section, the experimental setup and the results are presented and discussed in details.

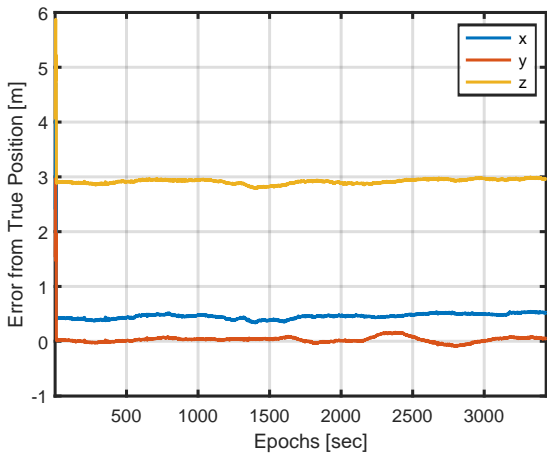


Fig. 19: RTK-Position error of Mi 8 without choke-ring



Fig. 20: Mi 8 choke-ring mounted on a rotating antenna

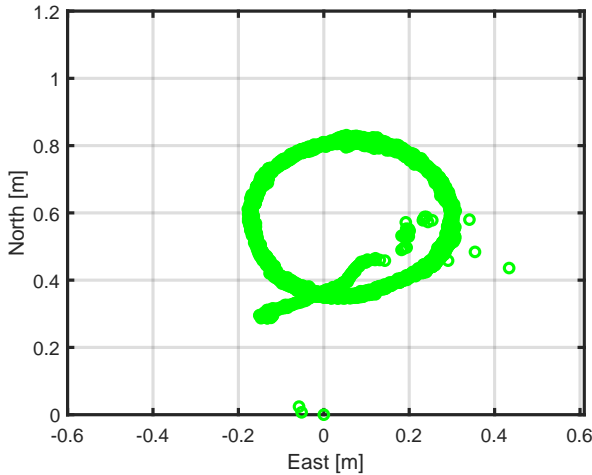


Fig. 21: Mi 8 RTK solution obtained from the setup in Fig. 20

A. Experimental Setup

Since the true position and orientation of the smartphone must be known very precisely (mm-accuracy and arc-second-accuracy), massive geodetic measurement pillars with very precise location and height information were used as a reference. These measurement pillars belong to the electronic distance measurement (EDM) calibration track in the *UniBwM*

campus. The deeply-grounded solid concrete pillars are continuously checked and adjusted (through a network adjustment) to have millimeter accuracy. A state-of-the-art total station, *Leica Nova MS60 MultiStation* [22], is used to determine the geometry and orientation of the smartphones in the global frame. Thanks to its highly precise angle and distance measurement, this instrument is able to deliver point accuracy in the millimeter range. According to the manufacturer specification [22], the obtained distance accuracy and the angular accuracy are $1 \text{ mm} + 1 \text{ ppm}$ and $1''$ (arc-second) respectively. As depicted in Fig. 22, the total station was placed directly on one pillar and oriented with a target prism mounted on another one (Fig. 22, top subfigure). With a distance between the total station and the measurement targets of less than 20 m, point accuracy of 1-2 mm can be expected accordingly. The formula below describes the classic polar attachment of a new point (P_N) from a known point (P_K). The measured direction is $t_{K,N}$ and the measured distance is expressed as $s_{K,N}$ (from P_K to P_N).

$$Y_N = Y_K + s_{K,N} \cdot \sin(t_{K,N}) \quad (3a)$$

$$X_N = X_K + s_{K,N} \cdot \cos(t_{K,N}) \quad (3b)$$

In order to be able to determine the geometry of the smartphones very precisely and to mount the devices firmly on the choke-ring, a support platform was produced with the help of a 3D printer. The corresponding 3D model was generated based on the specifications of the Xiaomi Mi 8 smartphone [23], so that the smartphones can fit perfectly. In addition, mounting locations for a Leica 360° mini prism (GRZ101) were integrated into this platform. The main advantage here, is that all dimensions can be calculated and taken directly from the 3D CAD-model. For example, the positions of the mountings for the prism are known very precisely with respect to the center of the platform (and thus the center of the pillar on which the choke-ring is mounted).

Now, the exact positions of the mounting frame can be measured by means of the total station. Since the position of the center point of the support platform is well known, namely that of the measurement pillar on which it is mounted together with the choke-ring, the rotation relative to this center is still missing in order to determine the absolute location and orientation. Fortunately, these offsets and misorientation can be easily determined with the help of corresponding points in the 3D-printed platform which are expressed in the Cartesian measurement system. The rotation angles are then estimated using a simple 2D rotation without translation (the measured points are considered relative to the coordinate of the pillar and thus relative to the center of the support platform) and scaling (we know that the platform does not experience any deformation). Please refer to Fig. 22, middle section. These rotation angles can be determined using the singular value decomposition (SVD) [24].

With the previous steps, the exact geometry of the smartphones can be obtained with good precision in a geodetic reference frame, nevertheless the location of the APC

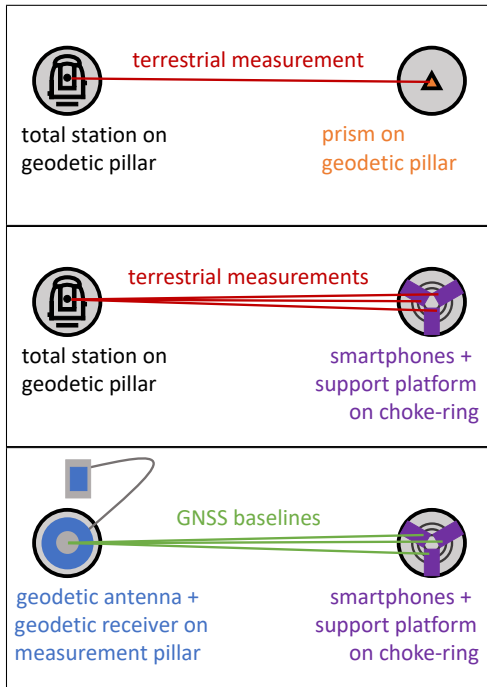


Fig. 22: Experiment setup for the exact determination of the smartphone APC location, to be interpreted from top to bottom



Fig. 23: Experiment setup with real environmental conditions for smartphone APC determination

within the smartphone housing is still unknown. To determine this parameter w.r.t. the geometry (smartphone body-frame), a static GNSS measurement campaign is conducted while keeping the previously determined position and orientation of the smartphones unchanged (Fig. 22, bottom part). Furthermore, to avoid any shadowing/reflection effects, we chose a measurement area with open sky conditions and, again, employed the choke ring platform as discussed in Section IV (see Fig. 23). With the help of the Trimble inc. forecast

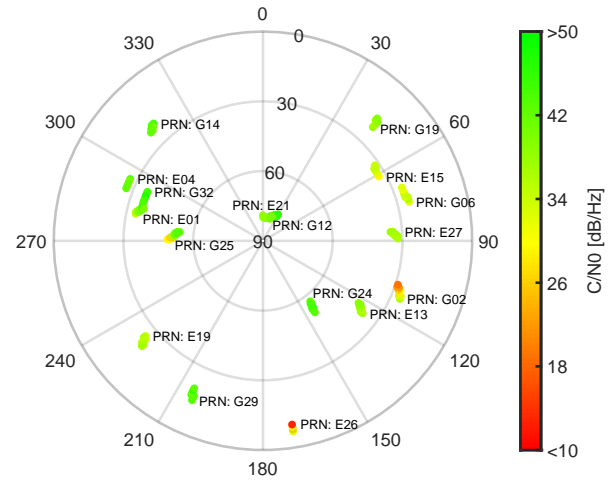


Fig. 24: Skyplot of the satellite visibility with the appropriate C/N0

software (*Trimble Online GNSS Planning tool* [25]), the best period for static GNSS measurement was selected to ensure the highest possible visibility of satellites, especially those satellites (GPS and Galileo) with an L5/E5A signal as they play a key role for fixing the ambiguity term. Based on this planing tool, the best constellations lasted for about 1 to 1.5 hours. Therefore, the GNSS raw observations were recorded using the *Geo++ RINEX Logger* (version 2.1.5) over a period of approximately 1 hour. The satellite visibility during the measurement campaign is displayed, exemplary for one single day, in the skyplot in Fig. 24.

Since a reference station with well known coordinates is always required to perform the RTK positioning, the same receiver and antenna used in the bus experiment (see Section. III) were installed on another pillar nearby. The baseline between the two pillars is approx. 18 meters. Thanks to this small baseline, the atmospheric influences is almost identical and consequently will be cancel out of the observation which enables a fast ambiguity fixing and also a short converges time of the RTK-position solution. Raw measurement data from both reference station and from the three smartphones were evaluated in post-processing using *Inertial Explorer*.

B. Experiment Results

Since the GNSS solution and the measured positions of the 3D-printed platform are expressed in the same Cartesian geodetic coordinate frame, namely UTM 32 (32 is the corresponding stripe for Germany), the linking of the data becomes very simple. An overview of the data generated in two consecutive days can be found in Fig. 25 and Fig. 26, where both sketches contain the same setup. Here, the model of support platform holding the three tested Mi 8 smartphones as well as a simplified representation of the choke-ring placed on top of the geodetic pillar is depicted. Based on the point clouds of the fixed RTK solutions for the three devices, ellipses were estimated in order to give statements about the

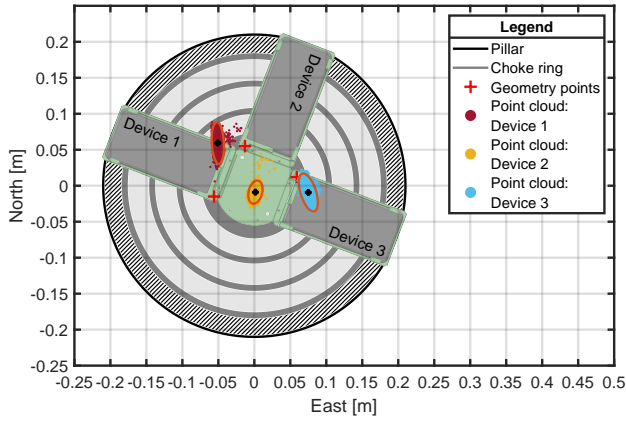


Fig. 25: Sketch of the experiment setup depicted in the UTM32 global frame, north-oriented and the pillar reference coordinates have been subtracted from the results, day 1

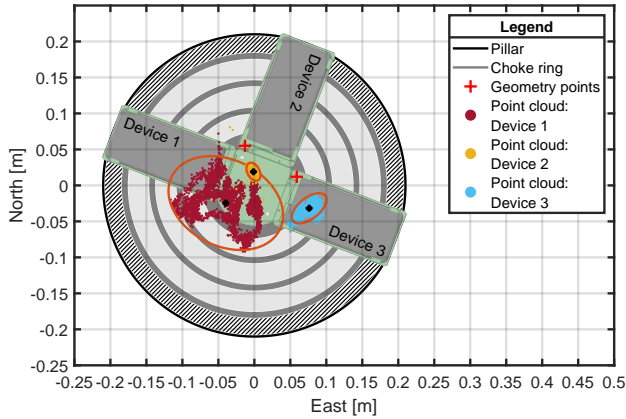


Fig. 26: Sketch of the experiment setup depicted in the UTM32 global frame, north-oriented and the pillar reference coordinates have been subtracted from the results, day 2

scattering of these point clusters w.r.t. the center. These ellipses correspond to the 95% confidence interval (2 sigma) of a 2D Gaussian distribution. The mean of these shapes is represented by the black dots. On the other hand, the exact location of screw holes (designed to host the Leica 360° mini prism) on the support platform are visualized by the red crosses.

Using the Leica MultiStation the obtained accuracy of the geometry of the support platform was around 2 mm, which is conform to the manufactures specifications [22]. However, the challenge here was to extract from the Mi 8 GNSS RTK-solution meaningful information that fit geometrically into the measured shape of this platform, i.e. the dimension and the orientation of the Xiaomi smartphones expressed in the UTM 32 projection frame. In the optimal case, the computed GNSS solution should represent a perfect ellipsoid which overlaps the smartphone's left upper corner, where the APC is assumed to be. This assumption is based on number of experiments we conducted, where the smartphone GNSS signal reception has been fully attenuated by only putting the finger on the

left upper corner of the device. In this experiment, the GNSS measurements collected in two different days, achieved an RTK fixing rates of over 95 %. These values strengthen the fact of repeatability of the obtained result. In order to guarantee a proper estimation of the phase center within the ellipsoids, only the fixed solutions were considered. With an average number of visible satellites of 14 (see satellite skyplot in Fig. 24, an elevation cut-off angle of 15° was applied) and a PDOP value of approx. 1.2, the measurement conditions were excellent. It should also be mentioned here that for the three tested smartphones, the behavior of the satellites in view were slightly different. This can happen due to the different orientation of the smartphones and the low quality of the antenna. As can be seen in Fig. 27, the point cloud for device $n^{\circ}1$ is not as dense as expected. The position also appears shifted between the two different days. This is because this smartphone had many cycle slips in the GNSS raw data which made the RTK-fixing procedure in the second day unpossible (Fig. 27, right plot). In addition, not all possible Galileo satellites in view have been tracked.

Fig. 27 to 29 show the point clouds in the smartphone coordinate system. As mentioned at the beginning, the transformation from the global system takes place via the estimated rotation of the support platform (with respect to the north direction) and the translation to the center of the smartphone, which is known from the 3D CAD model. The underlying transformation rule for rotation and translation in 2D is listed below:

$$\begin{bmatrix} x_{SM} \\ y_{SM} \end{bmatrix} = \begin{bmatrix} \cos(\alpha) & -\sin(\alpha) \\ \sin(\alpha) & \cos(\alpha) \end{bmatrix} \cdot \begin{bmatrix} E \\ N \end{bmatrix} + \begin{bmatrix} t_x \\ t_y \end{bmatrix} \quad (4)$$

Where α represents the rotation angle that rotates the east (E) and north (N) coordinates from the global frame to the local frame of the smartphone. t_x and t_y are the translation parameters. The calculated coordinates of the phase centers and the associated 2D point errors for the two days are shown separately in Table XIII and XIV. Here it is clear, that the variation in the two days (for devices $n^{\circ}2$ and $n^{\circ}3$) is relatively small and therefore the results have been confirmed. Also interesting is the different location of the estimated antenna phase centers: for the first device it is on the left upper corner, for the second device it is obviously outside and for the last device it is located centrally in the smartphone. This inconsistent APC behavior indicates that for absolute cm-accurate RTK positioning using smartphones, it is mandatory to further investigate those variations and possibly develop a calibration procedure if the variation are deterministic in nature. The 2D point error for all results (except the float solution for smartphone 1 on day 2) is in the expected RTK accuracy range of 2-3 cm. Similarly, the estimated height competent obtained during this experiment are depicted in Fig. 30 to 35, where the dark gray color represents the pillar, the bright gray color the choke-ring (real dimension) and the black layer on top is the smartphone thickness as defined by the manufacturer (7.6 mm). Assuming the absolute reference height (598.759 m) is crossing the middle of the smartphone (black layer), we

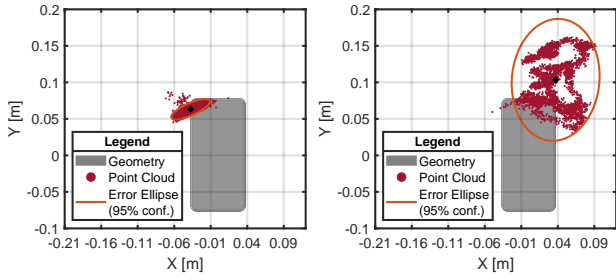


Fig. 27: Approximated APC from RTK-fixed solution from device $n^{\circ}1$ using two different data sets. day 1 (left) and day 2 (right, only float solution was possible)

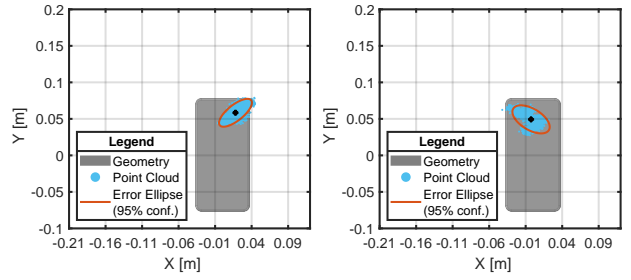


Fig. 29: Approximated APC from RTK-fixed solution from device $n^{\circ}3$ using two different data sets. day 1 (left) and day 2 (right)

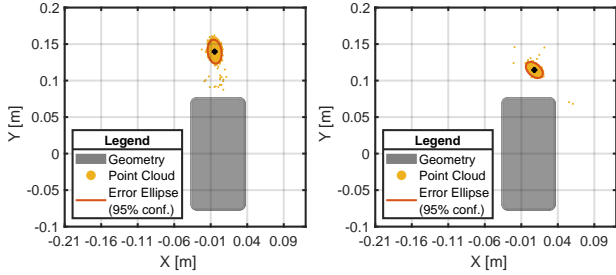


Fig. 28: Approximated APC from RTK-fixed solution from device $n^{\circ}2$ using two different data sets. day 1 (left) and day 2 (right)

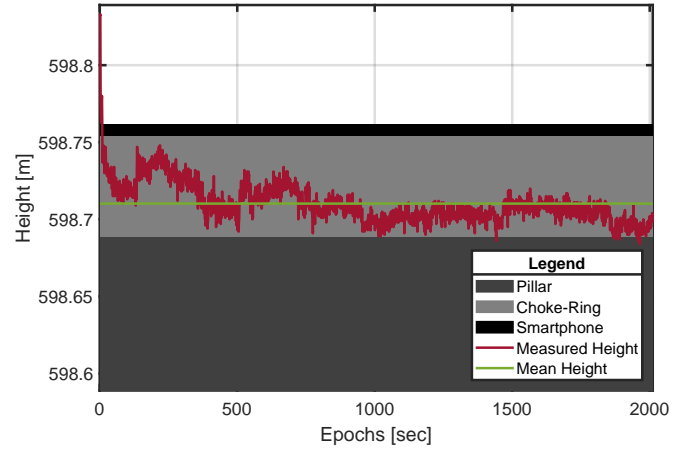


Fig. 30: Approximated APC height component from RTK-fixed solution for device $n^{\circ}1$, day 1

can assess the estimation accuracy of the APC along the z -direction. In general, the standard deviation (Table XV) of the height related to all smartphones is between 1.1 cm and 3.2 cm. The highest standard deviation value belongs to the Mi 8 device $n^{\circ}1$ in the the second day where only float solution was possible. Additionally, the fluctuation of this components shows a long term noisy signal. A remarkable result can be observed in Fig. 33 where the mean value of height passes exactly through the smartphone shape as the deviation of the estimated height (δh) w.r.t. the truth (middle of the smartphone) is in both days no more than 5 mm (Table XV). For device $n^{\circ}1$ and $n^{\circ}3$ in Fig. 30 to Fig. 31 and Fig. 34 to Fig. 35 respectively, the estimated height showed a very low accuracy, between 4.9 cm and 11.3 cm.

Henceforth, the APC for the three Mi 8 smartphones could be specified within this accuracy. It is clear that the accuracy in APC determination is not the same as for geodetic antennas, whose phase center is determined to some millimeters [19]. Nevertheless, our results prove that the low-cost *Broadcom* GNSS chips and the smartphone GNSS antennas make it possible to, reliably, achieve one decimeter accuracy.

CONCLUSION

The usefulness of multipath mitigation using choke-ring platform and its notable impact on positioning accuracy is quite evident. Even with the low quality antenna, smartphones are able to fix the ambiguities with high precision and accuracy. The smartphone position accuracy has been improved significantly from some meters (without choke-ring) up to

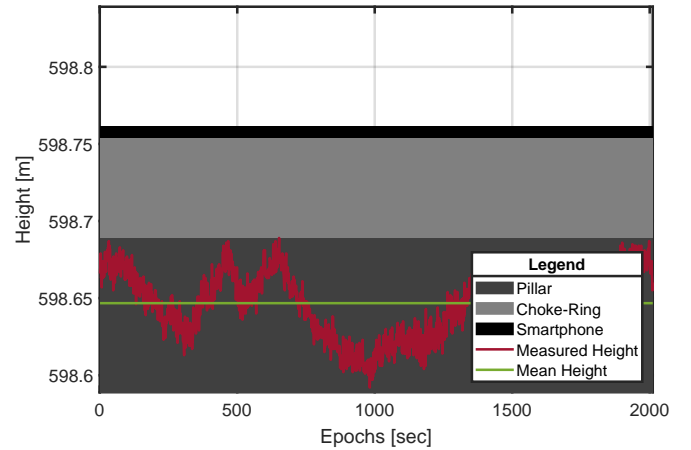


Fig. 31: Approximated APC height component from RTK-fixed solution for device $n^{\circ}1$, day 2 (only float solution was possible)

± 2 cm (with choke-ring). The phase center determination also demonstrate that, if precise antenna phase center variations (PCV) are known, the position accuracy can be further improved. However, it is required to do regressive test of the

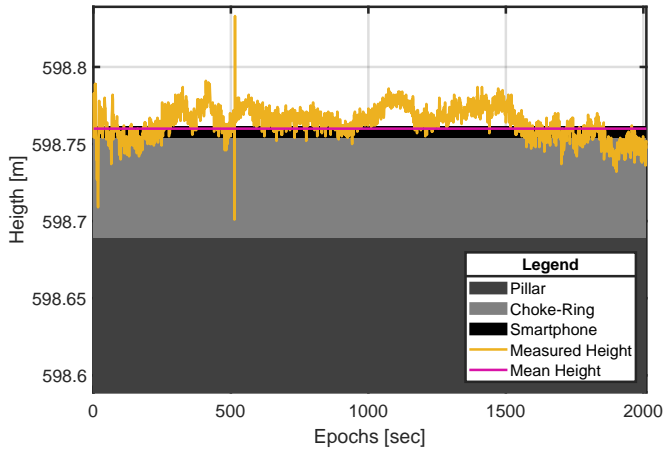


Fig. 32: Approximated APC height component from RTK-fixed solution for device $n^{\circ}2$, day 1

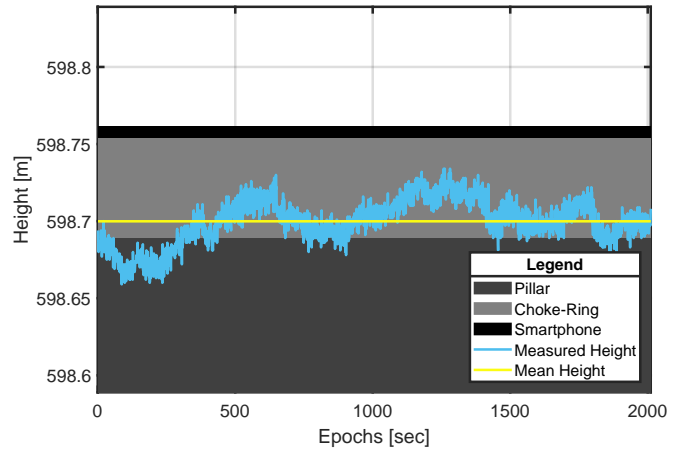


Fig. 35: Approximated APC height component from RTK-Fixed solution for device $n^{\circ}3$, day 2

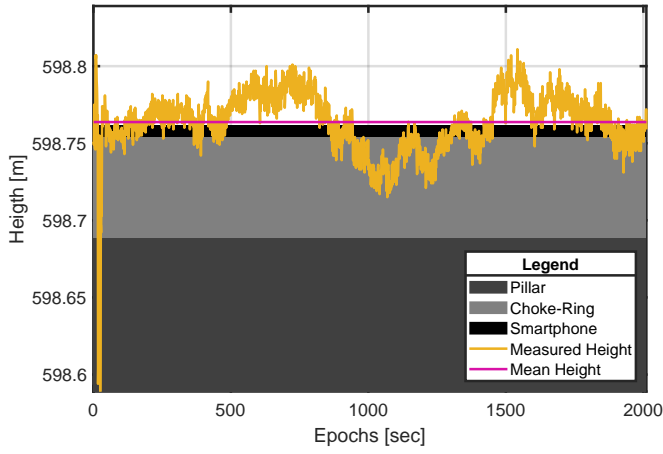


Fig. 33: Approximated APC height component from RTK-fixed solution for device $n^{\circ}2$, day 2

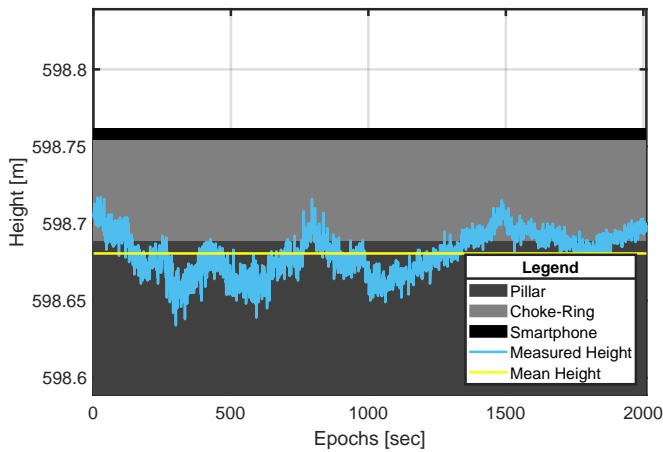


Fig. 34: Approximated APC height component from RTK-fixed solution for device $n^{\circ}3$, day 1

TABLE XIII: APC approximation accuracy, day 1

Smartphone	X [m]	Y [m]	2D-Error [m]
Mi 8 $n^{\circ}1$	-0.037	+0.063	0.030
Mi 8 $n^{\circ}2$	-0.004	+0.139	0.018
Mi 8 $n^{\circ}3$	+0.017	+0.058	0.029

TABLE XIV: APC approximation accuracy, day 2

Smartphone	X [m]	Y [m]	2D-Error [m]
Mi 8 $n^{\circ}1$	+0.037	+0.103	0.102
Mi 8 $n^{\circ}2$	+0.007	+0.114	0.015
Mi 8 $n^{\circ}3$	-0.002	+0.049	0.031

TABLE XV: APC height approximation accuracy

Smartphone	day 1		day 2	
	δh [m]	Std [m]	δh [m]	Std [m]
Mi 8 $n^{\circ}1$	0.049	0.013	0.113	0.020
Mi 8 $n^{\circ}2$	-0.005	0.010	-0.004	0.019
Mi 8 $n^{\circ}3$	0.079	0.014	0.059	0.014

phase center behavior with series of test campaigns to try and model the phase center variation for device under test (DUT) (smartphone). Additionally, the built-in MEMS IMU inside the Mi 8 smartphone shows, compared to commercial MEMS device, very reliable and steady behavior to be integrated into RTK fusion. For the future work, it is required to apply the Tightly-Coupling (TC) strategy to the smartphone GNSS and IMU observations for cycle slip detection and correction [17],

[26]. In addition to this, a software level multipath mitigation can also be tested with the smartphone data to avoid the bulky choke-ring platform.

ACKNOWLEDGMENT

The results presented in this work were developed within the project “Real-Time-Kinematic Positionierung am Mobiltelefon” (short: RAMBO) funded by the German Federal Ministry for Economic Affairs and Energy (BMWi) and administered by the Project Management Agency for Aeronautics Research of the German Space Agency (DLR) in Bonn, Germany (grant n°. 50NA1720).

REFERENCES

- [1] GSA, “Report on location-based services user needs and requirements,” 2019. [Online]. Available: https://www.gsc-europa.eu/sites/default/files/sites/all/files/Report_on_User_Needs_and_Requirements_LBS.pdf
- [2] H. Sharma, A. Schütz, and T. Pany, “Qualitative analysis of smartphone GNSS raw measurements and effect of duty cycling on the RTK positioning,” in *NAVITEC*, Noordwijk, The Netherlands, 2018.
- [3] H. Sharma, M. Bochkati, G. Kestel, and T. Pany, “Researchers achieve 1–2 cm accuracy with commercial smartphone,” *Inside GNSS*, 2019.
- [4] L. Wanninger and A. Heßelbarth, “GNSS code and carrier phase observations of a Huawei P30 smartphone: quality assessment and centimeter-accurate positioning,” *GPS Solutions*, vol. 24, no. 2, p. 64, Apr. 2020. [Online]. Available: <https://doi.org/10.1007/s10291-020-00978-z>
- [5] N. Aboelmagd, B. K. Tashfeen, and J. Georgy, *Fundamentals of Inertial Navigation, Satellite-based Positioning and their Integration*. Springer Berlin Heidelberg, 2012.
- [6] Google, “GPS Measurement Tools.” [Online]. Available: <https://github.com/google/gps-measurement-tools>
- [7] A. Vydhyanathan and G. Bellusci, “The next generation Xsens motion trackers for industrial applications,” *Xsens: Enschede, The Netherlands*, 2015.
- [8] Google, “Android Developers - SensorManager.” [Online]. Available: <https://developer.android.com/reference/android/hardware/SensorManager>
- [9] D. Allan, H. Hellwig, P. Kartaschoff, J. Vanier, J. Vig, G. Winkler, and N. Yannoni, “Standard Terminology for Fundamental Frequency and Time Metrology,” 1998.
- [10] “IEEE Standard Specification Format Guide and Test Procedure for Single-axis Laser Gyros,” *IEEE Std 647-1995*, pp. 1–88, May 1996.
- [11] A. Gelb, *Applied Optimal Estimation*, A. S. C. T. Staff, Ed. MIT Press Ltd, 1974.
- [12] S. Nassar, “Improving the inertial navigation system (INS) error model for INS and INS/DGPS applications,” PhDthesis, Department of Geomatics Engineering, University of Calgary, Canada, Calgary, Alberta, Nov. 2003.
- [13] D. Titterton and J. Weston, *Strapdown Inertial Navigation Technology, Second Edition (Progress in Astronautics and Aeronautics)*. AIAA, 2005.
- [14] S. J. Dixon-Warren. (2010) Motion sensing in the iPhone 4: MEMS accelerometer. *MEMS Journal*. (Accessed on 2020-03-12). [Online]. Available: <https://www.memsjournal.com/2010/12/motion-sensing-in-the-iphone-4-mems-accelerometer.html>
- [15] H. Sun, D. Fang, K. Jia, F. Maarouf, H. Qu, and H. Xie, “A low-power low-noise dual-chopper amplifier for capacitive CMOS-MEMS accelerometers,” vol. 11, no. 4, pp. 925–933, Apr. 2011.
- [16] NovAtel Inc., *Inertial Explorer 8.70 User Manual*, 2018. [Online]. Available: <https://www.novatel.com/assets/Documents/Waypoint/Downloads/Inertial-Explorer-User-Manual-870.pdf>
- [17] P. D. Groves, *Principles of GNSS, Inertial, and Multisensor Integrated Navigation Systems, Second Edition*, ser. GNSS/GPS. Artech House, 2013.
- [18] M. Becker, P. Zeimet, and E. Schönemann, “Anechoic chamber calibrations of phase center variations for new and existing GNSS signals and potential impacts on IGS processing,” in *IGS workshop*, Newcastle Upon Tyne, GB, 2010. [Online]. Available: <http://www.igs.org/presents/workshop2010>
- [19] T. Kersten and S. Schön, “Receiver antenna phase center models and their impact on geodetic parameters,” in *International Symposium on Earth and Environmental Sciences for Future Generations*, J. T. Freymueller and L. Sánchez, Eds. Cham: Springer International Publishing, 2018, pp. 253–259.
- [20] EM Devices, “Rotation unit with power box,” 2020, unpublished. [Online]. Available: <http://www.em-devices.eu/>
- [21] Geo++ GmbH, “Geo++ RINEX Logger.” [Online]. Available: <http://www.geopp.de/logging-of-gnss-raw-data-on-android/>
- [22] Leica Geosystems AG, *Leica Nova MS60 Data sheet*, 2015. [Online]. Available: https://w3.leica-geosystems.com/downloads/123/zz/tps/nova_ms60/brochures-datasheet/Leica%20Nova%20MS60%20DS_en.pdf
- [23] Xiaomi Tech. (2020) Mi 8 Specifications. (Accessed on 2020-04-13). [Online]. Available: <https://www.mi.com/global/mi8/specs>
- [24] K. S. Arun, T. S. Huang, and S. D. Blostein, “Least-squares fitting of two 3-D point sets,” *IEEE Transactions on Pattern Analysis and Machine Intelligence*, vol. PAMI-9, no. 5, pp. 698–700, Sep. 1987.
- [25] Trimble Inc. (2018) Trimble GNSS planning online. (Accessed on 2020-01-20). [Online]. Available: <https://www.gnssplanning.com>
- [26] T. Takasu and A. K. Yasuda, “Cycle slip detection and fixing by MEMS-IMU/GPS integration for mobile environment RTK-GPS,” in *Proceedings of the 21st International Technical Meeting of the Satellite Division of The Institute of Navigation (ION GNSS 2008)*, Savannah, GA, September 2008, pp. 64–71.